JMEPEG (2019) 28:7016–7024
https://doi.org/10.1007/s11665-019-04416-1

1059-9495/$19.00

Characterization of Subsurface Microstructural Alterations Induced by Hard Turning of Inconel 718

Heithem Touazine, Kanwal Chadha, Mohammad Jahazi, and Philippe Bocher

(Submitted February 3, 2019; in revised form October 15, 2019; published online November 4, 2019)

Conventional machining especially hard turning is commonly used in aerospace industry to produce the final shape of cylindrical parts. However, the process generates damages and microstructural alterations on the surface and at the subsurface layer, in particular the cracking of hard carbides particles. The present paper focuses on investigating the probable mechanisms responsible for carbide cracking and the formation of a softened layer at a depth between 10 and 30 µm below the machined surface. Advanced techniques, such as laser confocal microscopy and field emission gun scanning electron microscope equipped with in situ picoindenter and electron backscatter diffraction, were used to characterize and analyze the evolution of the microstructure in the affected layer and propose the possible governing mechanisms for the observations.

Keywords cracked carbides, EBSD, hard turning, in situ SEM picoindenter, KAM, nanohardness, soft layer, subsurface damage

1. Introduction

Inconel 718 is one of the most used superalloys in the aerospace industry for the fabrication of turbine disks, blades and shafts. It covers more than 50% of the aircraft engine especially the hot section (Ref 1) due to its superior properties such us resistance to corrosion, oxidation and creep (Ref 2-5) at high temperatures up to 650 °C (Ref 6, 7). The good properties of Inconel 718 are due to the presence of secondary phases such gamma prime γ' Ni_3 (Al, Ti), gamma double prime γ'' (Ni_3Nb) and the delta δ. The microstructure contains also hard particles such us titanium and niobium carbides (Ti, Nb) C located within the grains and at the grain boundaries (Ref 5). The presence of the carbides improves creep resistance and in combination with delta phase contributes to preventing grain growth at high working temperatures (Ref 2, 5). However, machining of Inconel 718 presents many challenges mainly due to the significant work hardening and the presence of (Ti, Nb) C carbide particles in the microstructure (Ref 8, 9). In fact, the hard carbide particles produce abrasive wear on the cutting tools (Ref 8, 10, 11) which induces surface damages and discontinuities in the machined surface and subsurface layers (Ref 8, 10, 12). Such damages to the surface integrity could result in reduced service life, and if very severe, they could lead to the scrapping of the finished component (Ref 13, 14).

Most of the existing studies have focused on tool wear (Ref 11, 15-18) or the influence of cutting parameters on surface integrity, especially on roughness (Ref 19-23) and residual stresses evolution (Ref 24-28). Only few studies have investigated the effect of machining parameters on microstructure evolution of superalloys (Ref 26-29) and particularly on the mechanisms responsible for microstructure alterations. For example, Ranganath et al. (Ref 29) and Long et al. (Ref 30) studied the impact of machining process and tool geometry parameters on carbide cracking in superalloys. They found that sharp tool, small nose radius and small feed rate decrease the amount of the cracked and scattered carbides. But, no explanation was provided about the mechanisms responsible for carbide cracking. In a recent study, Touazine et al. (Ref 31) proposed a model to predict the evolution of cracked carbides as a function of machining parameters. It was shown that the amount of cracked carbides increased with increasing material removal rate and deformation energy. On the other hand, Sharman et al. (Ref 28) reported the presence of a softened layer in the subsurface of a machined Inconel 718. They observed a hardness drop and related it to thermal softening and relaxation of residual stresses under the effect of temperature. Similar results based on microhardness profiles were reported by the present authors on an Inconel 718 (Ref 32). The depth of the softened region was between 10 and 30 µm beneath the machined surface.

The possible causes for the cracking of (Ti, Nb) C carbides and the presence of a softened layer in the subsurface of machined Inconel 718 samples remain still to be clarified. The present study will focuses on further characterizing these two phenomena and discuss the possible mechanisms responsible for their occurrence. The experimental investigation was carried out using FEG-SEM equipped with EBSD backscatter diffraction and in situ picoindenter.

2. Materials and Methods

Inconel 718 samples were heat-treated according to the AMS 5663 standard resulting in a 47 HRC hardness level. The nominal chemical composition of the investigated superalloy is presented in Table 1. It should be noted that MC carbides are not dissolved during the AMS 5663 heat treatment process.

Heithem Touazine, Kanwal Chadha, Mohammad Jahazi, and **Philippe Bocher**, École de technologie supérieure, Montreal, Canada. Contact e-mail: heithem.touazine@gmail.com.

Table 1 Chemical composition of the investigated superalloy (wt.%)

Element	Ni	Fe	Cr	Nb	Ti	Mo	V	Al	Ta	Si	C
wt.%	52.97	18.51	18.36	4.47	1.02	3.14	0.09	0.39	0.22	0.22	0.07

Specimens were machined using MAZAK-NEXUS CNC center with uncoated tungsten carbide under finishing regime. In the present study, selected samples were analyzed using EBSD and nanoindentation techniques based on a design of experiments (DOE) plan, the details of which were presented in a previous publication (Ref 31). The grain size was measured according to ASTM E112-13 to be 20 μm. The specimens were sectioned from 51-mm-diameter bar using wire electrical discharge machining in order to reduce mechanical damage and distortion in the machined surface. Before metallographic preparation, the machined samples were coated with pure nickel coating in order to protect the surface during polishing operation (Ref 32).

The effect of machining on subsurface damage and the location of cracked carbides with respect to the machined surface were examined on mirror polished samples using an OLYMPUS LEXT OLS 4100 laser confocal microscope and a Hitachi SU-8230 FEG-SEM. In addition, image analysis was performed using OLYMPUS LEXT OLS 4100 to determine the distribution of the carbide sizes on the as-received Inconel 718 microstructure. The maximum depth of the affected layer by machining was determined to be 30 μm (Ref 31). In the present investigation, all the carbides present in a depth of 30 μm were analyzed; however, in order to reduce the counting error only carbides larger than 3 μm were considered. For EBSD analysis, the samples were polished mechanically using conventional techniques and then electropolished at room temperature using a mixture of perchloric acid and ethanol (1:9 by volume). The electropolishing was carried out at 25 V for 15 s. The EBSD analysis and Schmidt factor distribution maps were performed using Burker EBSD software on the Hitachi SU-8230 FEG-SEM.

Nanoindentation tests were performed using Hysitron PI 88 SEM Picoindenter plugged inside scanning electron microscope chamber, as shown in Fig. 1(a) and (b). A single indentation was applied in each grain as illustrated in Fig. 1(c). For each depth, an average of five measurements for hardness and displacement was taken The indentations were performed with 15 mN load, 5 s charging time, 5 s holding time and 5 s discharging time, as shown in Fig. 2.

2.1 Distribution and Location of Cracked Carbides

The as-received material contains 2.6% of cracked oriented randomly through the microstructure, as shown in Fig. 3(a) and (b). The major causes of cracks are deformation during forging of the ingots or heat treatments, as also reported by Texier el al. (Ref 33). A previous work indicated that the amount of cracked carbides increases with increasing material removal rate and deformation energy during machining of Inconel 718 (Ref 31).

In addition, the microstructure presents different sizes of (Ti, Nb) C carbides, as shown in Fig. 4. To draw a representative distribution of carbide size of the studied material, more than 6000 carbides were analyzed using image analysis technique

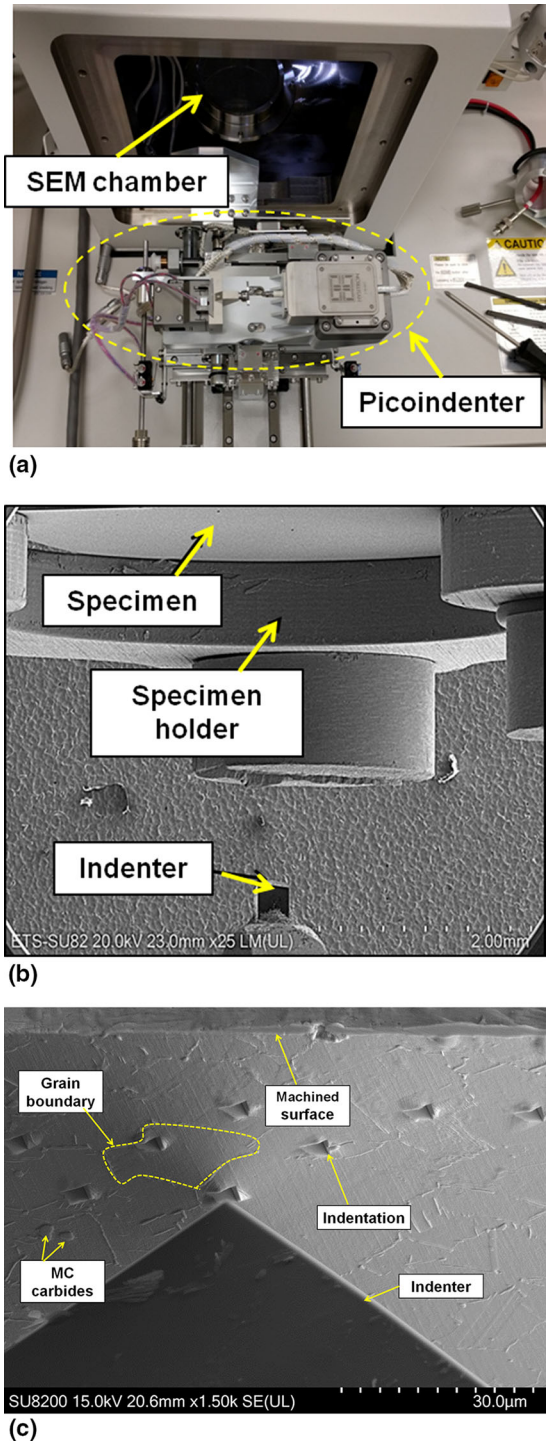

Fig. 1 Hysitron PI 88 SEM picoindenter: (a) plugging of the picoindenter inside SEM chamber, (b) indentation and imaging at real time and (c) nanoindentation performed at the real time allowing us to avoid hitting (Ti, Nb) C carbides

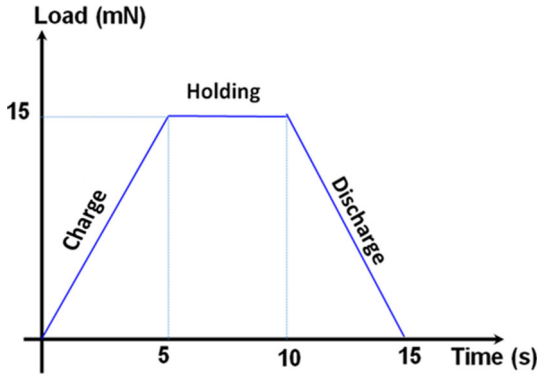

Fig. 2 Performed nanoindentation cycle

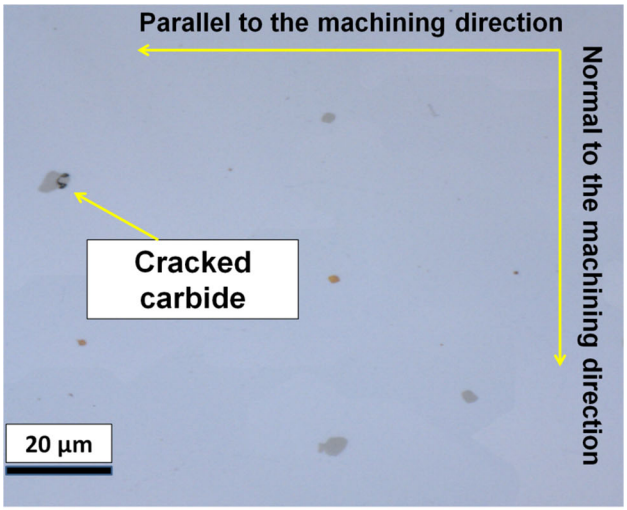

(a)

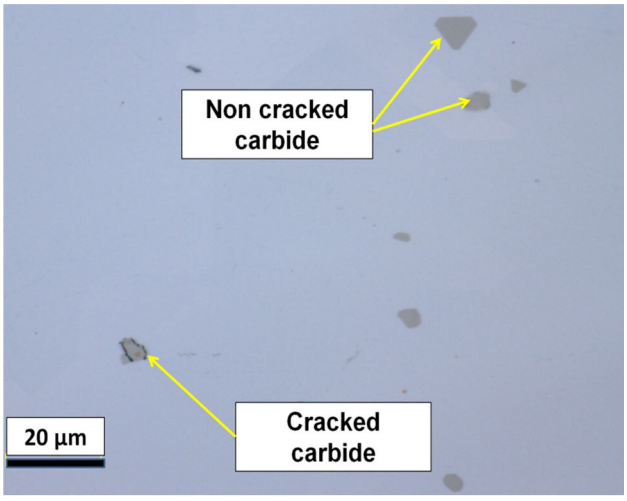

(b)

Fig. 3 Different types of cracked carbides in the as-received material

with a lens of 50× magnification. The results indicated that 76% of carbides were less than 3 µm, as shown in Fig. 5. It should be mentioned that in a previous study (Ref 31) it was shown that the amount of cracked carbides changed with changing the cutting parameters. In the present study, the possible mechanisms responsible for the formation of cracked

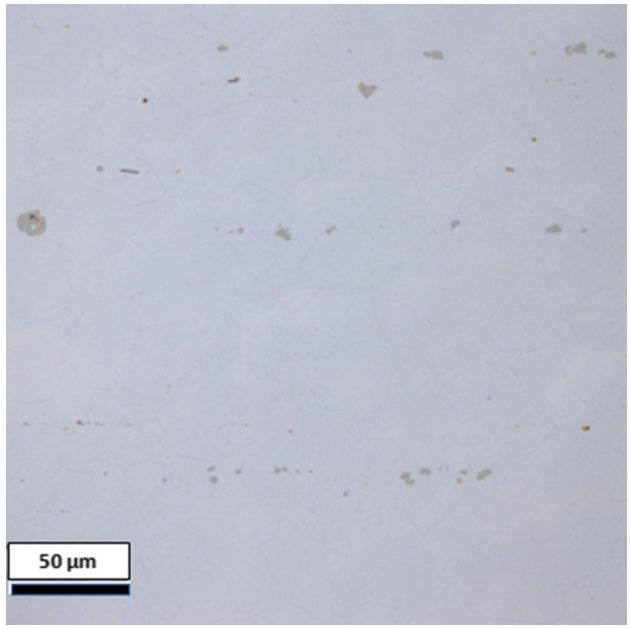

Fig. 4 Different sizes of carbides in the as-received material with 50× magnification lens

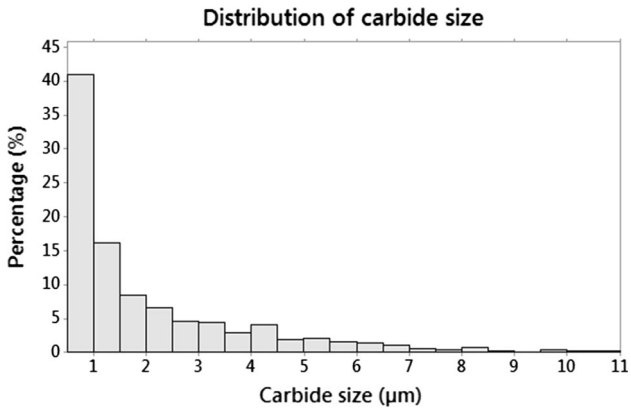

Fig. 5 Carbide size distribution in the microstructure of Inconel 718

carbides under 'finishing' regime (i.e., very 'smooth' damage to the microstructure) were investigated.

Optical microscopy was used to distinguish between cracked and non-cracked carbides under different finishing cutting conditions, as presented in Fig. 6(a), (b) and (c). The related cutting conditions [i.e., cutting speed V_c (m/min), feed rate f (mm/rev) and depth of cut DoC (mm)] are presented in Table 2. In general, the analyses showed that carbides comprised between 0.5 and 3 µm were not cracked.

The thickness of the deformed layer was measured from the surface to the last distorted grain boundary and to the last defect, including cracked carbides. To this end, at least five measurements were taken and the average was taken and used in the analysis. Microscopic examination of the subsurface layer did not reveal any specific distribution of carbides, whether cracked and non-cracked ones. Figure 6(a), (b) and (c) shows some illustrative examples, where it can be seen that the cracked carbides are below the non-cracked one (Fig. 5(a), while in Fig. 6b, the cracked carbide is seen below few non-

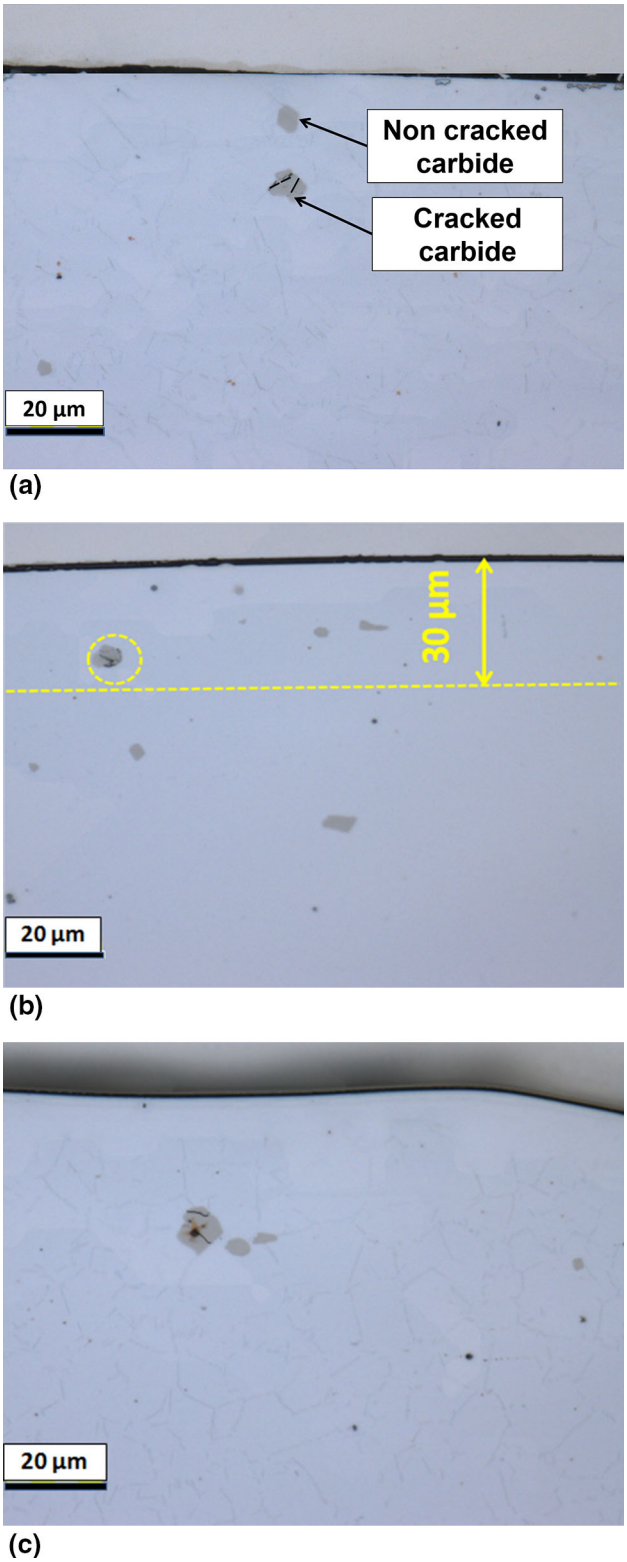

Fig. 6 Example of cracked carbides after machining of Inconel 718: (a) maximum depth of the analyzed surface, (b) typical cracked carbide located at 23 µm beneath the machined surface and (c) large-sized carbides are easier to fracture

cracked ones with a size less than 3 µm, and lastly, in Fig. 6(c) the cracked carbide is seen above all non-cracked ones. Thus, there is no consistency in the presence of cracked carbides with respect to the depth beneath the machined surface. Also, the microscopic analysis indicated that the majority of the cracked carbides were located in a depth comprised between 12 and 23 µm beneath the machined surface for different cutting conditions as shown in Fig. 6(a), (b) and (c). A similar behavior was found by Ranganath et al. (Ref 34) and by Guo and Anurag (Ref 35). They explained that the carbide cracking occurs simultaneously with the rotation along the cutting direction during material removal process for the large-sized carbides, whereas small carbides flow with the material and rotate along the cutting direction without cracking.

Table 2 Different cutting conditions related to the analyzed samples

Run	Figures	V_c, m/min	f, mm/rev	DOC, mm
a	6	67	0.264	0.230
b	7, 8 et 9	58	0.142	0.265
c	10	49	0.264	0.300

2.2 EBSD Analysis

Figure 7(a) and (b) shows the image quality (IQ) maps of two random locations of machined Inconel 718 sample. The black lines in the images denote high-angle grain boundaries (HAGB, $\theta > 15°$). The machined surface can be seen in the top region of the IQ map which is concentrated below 10 µm of the surface. The IQ maps depict a clear visualization of the presence of carbides located in the subsurface layer. Using EBSD technique, grains and carbides could be distinguished based on the crystallographic structure and lattice parameters (Ref 36). The presence of cracked carbides along with the non-cracked ones can be seen very clearly. Similar observations are shown in Fig. 6(a), (b) and (c) where cracked carbides were visible at different depths and locations. IQ maps provide a very clear image of cracks and grains and their misorientation relation with respect to the neighboring ones, as shown in Fig. 7(a) and (b). However, it is still difficult to predict the reason for the presence of cracked carbides along with the non-cracked ones with respect to the depth beneath the machined surface.

EBSD maps (Fig. 8) showing distribution of Schmid factor beneath the machined surface were generated by considering the direction of compression as perpendicular to the transverse direction of the machined sample. These maps represent high and low values of the Schmid factor which indicate that the grains are soft and hard, respectively (Ref 37). As illustrated in Fig. 8(a), (b) and (c), most of the grains in the as-received and the machined material have a relatively high Schmid factor of more than 0.4 and the distributions of Schmid factors were slightly different for the two zones of the same machined sample. In addition, Schmid factor maps showed that the grains in the affected layer by machining present a gradient of Schmid factor under the effect of deformation induced by machining. It was observed from the maps that the preferential location of crack initiation in the carbides was at the boundaries of grains which presented a gradient of Schmid factor. However, the carbide encircled in black in Figure 8(a) was not cracked probably because it was located outside the affected area by machining. It was surrounded with non-deformed grains which do not present a gradient of Schmid factor as demonstrated by

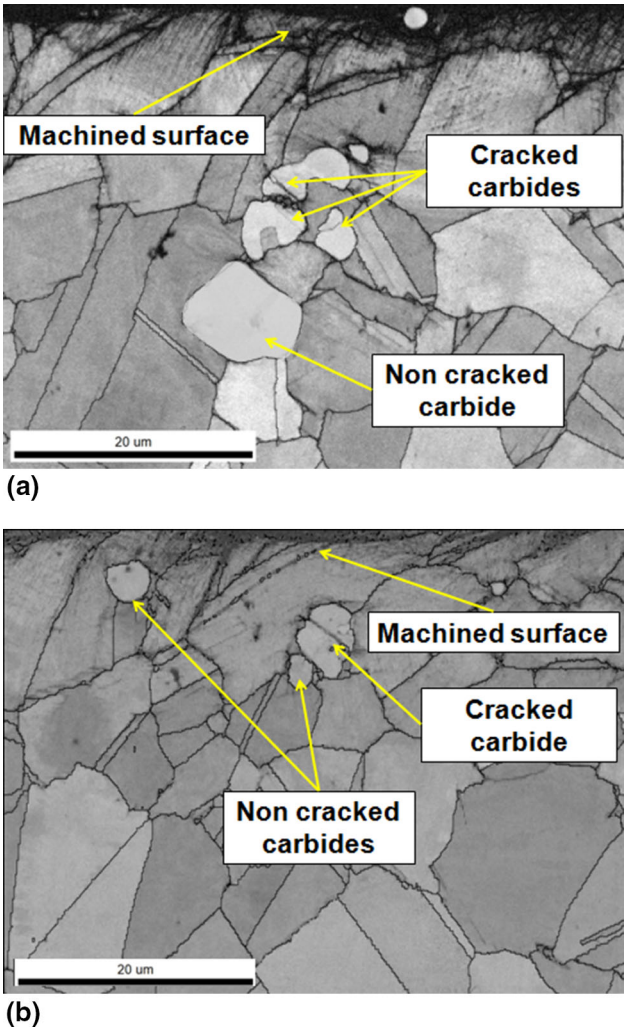

Fig. 7 IQ images of machined Inconel 718 surface showing the presence of cracked and non-cracked carbides

the uniform color of the grains around the circled carbide shown in Fig. 8(a). Furthermore, it can be observed that the carbides located at the grain boundaries are the ones which are easiest to be cracked, as shown in Fig. 7(b) and 8(b).

The relation between cracked carbides formation with the gradient of the Schmid factor of grains adjacent to cracked carbides probably indicates that the cracking process is related to a dislocation accumulation and grain orientation. In those boundaries, dislocations are expected to be piled up at grain boundaries with a large difference in Schmid factor as a result of the blocking of slip systems (Ref 38-40).

Observation of the cracked carbides in the subsurface region showed that almost all the *cracks* had a 45° angle with the machined surface (i.e., the horizontal line). This is in contrast to those in the as-received material, which did not show any preferential orientation, as indicated above and shown in Fig. 3(a) and (b). This finding suggests that the deformation of the material during machining brings the larger precipitates to cleave under the maximum resolved shear stress (45°) due to the large difference of deformation path between the top and the bottom of the carbides. On the other hand, the smaller carbides flow with the deformed matrix and therefore do not necessarily crack. Agrawal et al. (Ref 41) and Lee (Ref 42) reported

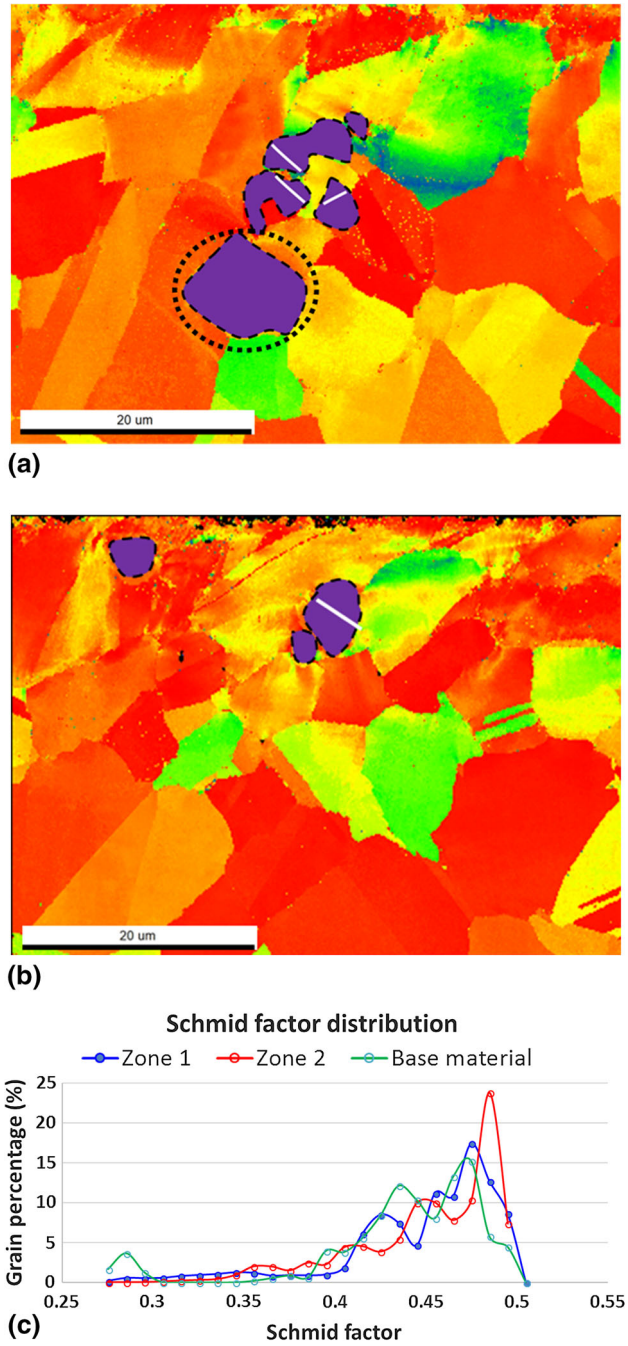

Fig. 8 EBSD maps showing the distribution of the Schmid factor in the machined Inconel 718 in the compression direction: (a) zone 1, (b) zone 2 and (c) Schmid factor distribution for zone 1, zone 2 and base material

observed similar behavior in aluminum alloys. On the basis of the above findings, the rotation of carbides during material removal process combined with the higher dislocation density caused by the gradient of Schmid factor of grains adjacent to the carbides could initiate and facilitate the cracking. In order to further analyze the grains adjacent to the cracked carbides, kernel average misorientation (KAM) maps were generated using TSL-OIM™ software. Figure 9 shows a high-magnification EBSD maps. Green and blue colors represent, respectively, high and low KAM values. It confirmed that the gradient of KAM and Schmid factor can be easily observed around the

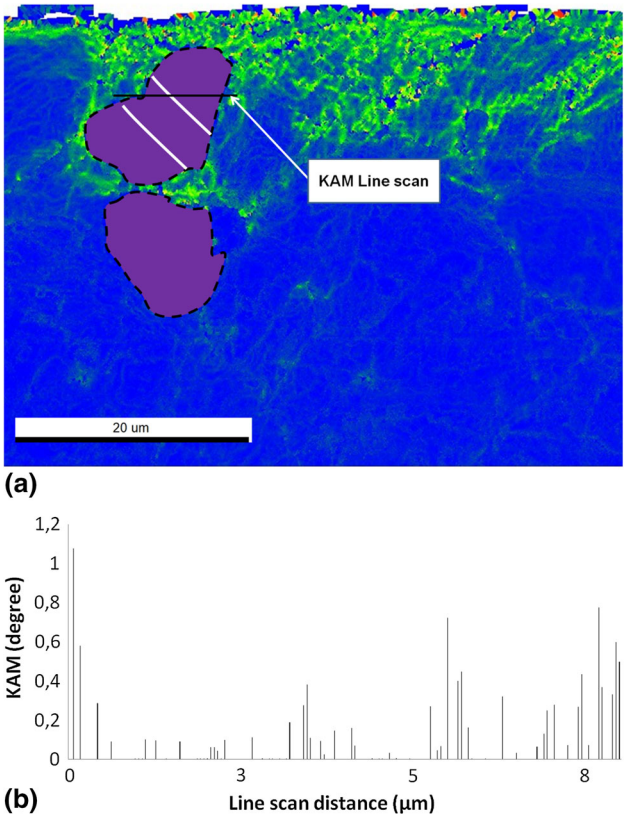

Fig. 9 EBSD maps showing the high gradient of Schmid factor and KAM around the cracked carbides: (a) KAM map and (b) line scan KAM values

cracked carbide. The higher KAM around the carbide can lead to high stresses which ultimately result in the cracking of the carbide. A line scan was performed in the cracked carbide circled in black as shown in Fig. 9(a). Using line scan, KAM values were drawn from the left to the right as shown in Fig. 10(b). KAM values across the matrix/carbide interface indicated a significant presence of dislocations around the carbide. Also, we can conclude that the distribution of KAM in the matrix did not present a gradient around them, most likely because the material has recrystallized after the forging operation. It is different for the affected layer by machining.

In this context, as also reported by Révilla et al. (Ref 43) KAM measurements can provide quantitative information about the dislocation density present in the matrix. The level of KAM (degree) within the grain gives the level of dislocation density in them. In the KAM analysis, higher is the dislocation density (or in other words strain), higher will be the KAM value (Ref 44, 45). Figure 10(a) and (b) shows the KAM maps of the random image of Inconel 718, where it can be seen that the KAM is higher near the machining surface, as compared to further depths. These results are similar to the ones reported by Zhang et al. (Ref 46) who found that KAM values were higher near the machined surface because of plastic deformation and were lower through the thickness. The present study shows that cracks on carbides appeared to be initiating at zones where the KAM gradient values were between 12 and 25 µm, i.e., higher dislocation density at the interface carbide/grain (Fig. 9a). The crack (encircled in white color) initiates from the left side of the carbide, which is red in color indicating high KAM, whereas on the right side of the grain, relatively low levels of KAM can be

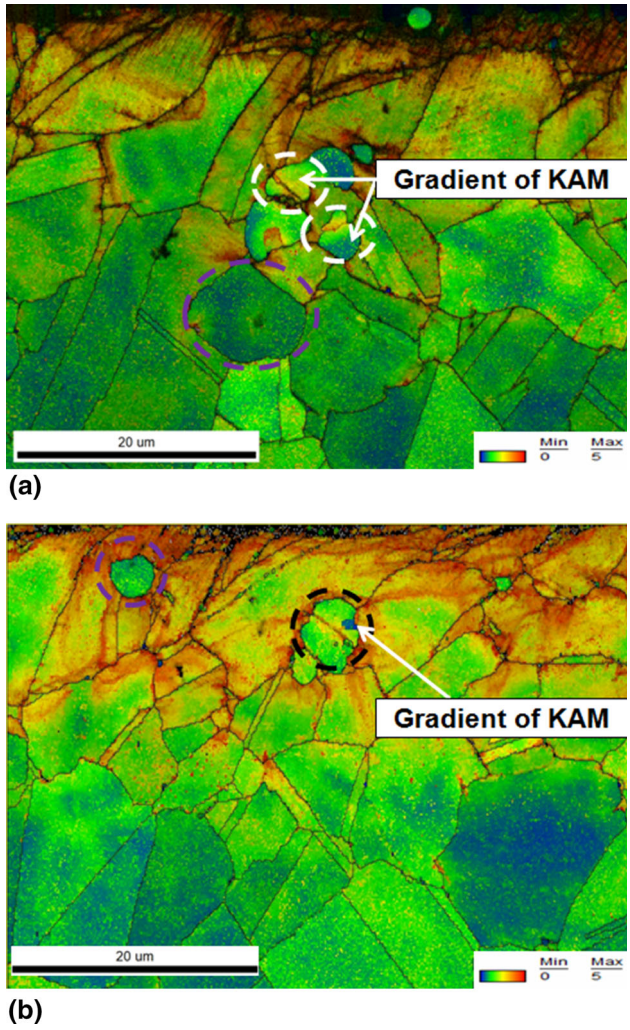

Fig. 10 Kernel average misorientation maps of machined Inconel 718 samples

seen. Likewise in Fig. 9(b), similar observation is made from the cracked carbide (encircled in black color), where the presence of two gradients can be observed, i.e., high KAM on the left side of the carbide and relatively low KAM on the right side but not within the carbide (shown with white arrows).

The observations in Fig. 10(a) and (b) give a probable indication that the cracks are initiating when there is a sharp gradient of dislocation density at the edges of the carbides.

The proposed mechanism holds strong with the observation of the non-cracked carbides [encircled in violet in Fig. 10(a) and (b)] where the surrounding areas of these carbides do not show the presence of a KAM gradient or high Schmid factor values. However, a question could arise whether the high KAM value is a cause for carbide cracking or is a consequence of it. In a previous research (Ref 32), the present authors found high misorientations around carbides in non-deformed Inconel 718. Also, in a recent research, Graboulev et al. identified high-KAM regions as potential locations for microcrack initiation in steel samples submitted to fatigue testing (Ref 47). The above findings support the view that high KAM values could be the cause for carbide cracking in the investigated material.

However, for some grains located near the machined surface the correlation between high Schmid factor and low dislocation density is not fully respected, as shown in Fig. 8(a) and (b) and

10(a) and (b). Birosca (Ref 37) in their study of deformation of RR1000 nickel-based superalloy also observed a similar behavior for some grains. For example, they found that in general high Schmid factors (between 0.42 and 0.5) were associated with geometrically necessary dislocation (GND) of about $10^{2.4}/\mu m^2$, while for lower Schmid factor values the GND was about twice higher. On the other hand, for some grains they found irregularities as in the present case. No specific reason was provided for the observed deviations.

2.3 Nanohardness Evolution

Nanoindentations were performed with the objective to investigate the presence of a softened layer at the machined subsurface using Berkovich indenter from the machined surface to the bulk material. For each indentation, depth of indentation and hardness values were measured and five measurements were taken for the same depth. Hardness is defined by dividing the maximal indentation load (P_{max}) by maximal projected contact area (A_{max}) as shown by the following equation:

$$H = \frac{P_{max}}{A_{max}}$$

Thanks to the picoindenter device, the (Ti, Nb) C carbides present in the microstructure of the Inconel 718 were avoided in order to measure the material hardness and to reduce the standard deviation of measurements. The results are reported in Fig. 11 where the hardness evolution is reported by the blue curve and the indentation depth with the red curve. The hardened layer has a depth of about 12 µm and 0.4 GPa harder than the bulk material. The dispersion for the hardness values suggests a heterogeneous deformation throughout the machined surface, which may be related to different orientations and hardnesses of the grains in the as-received material. The hardness then drops, and a 10-µm-thick layer softer than the bulk material with 0.35 GPa is observed. Simultaneously, the depth of the indentations (displacement) was measured. The obtained values confirm the presence of both a hardened layer and a softened layer with displacements of the order of 1980 nm in the first 12 µm and of between 2050 and 2125 nm of depth between 12 and 23 µm. This enhancement of hardness just below the surface is directly related to the work hardening and the plastic deformations induced during machining. The hardened region is characterized by intense deformation of grains and deflection of grain boundaries due to the tool pressure and material shearing. The 12 µm thickness of the hardened layer was confirmed with the KAM maps which showed a high concentration of local misorientation represented in red color in Fig. 10(a) and (b).

Previous research (Ref 28) reported that the softening in the subsurface layer could be related to the thermal softening and residual stress relaxation. Two different techniques could be used to measure residual stresses, namely magnetic Barkhausen noise and eddy current residual stress profiling. The first method is an effective technique to validate the presence of tensile residual stresses as well as applied tensile stresses on ferromagnetic materials. However, this technique is extremely sensitive to microstructural variations (gradients), and for high stress levels, near the yield limit of the tested material, a saturation of the magnetic Barkhausen noise occurs. This fact suggests a limitation in the use of this test method for absolute measurements in our case as microstructural gradients are generated due to severe machining conditions (Ref 48). For the second method, the nature of material could present a capability limitation.

In order to evaluate the possible microstructural changes in the subsurface, the evolution of nanohardness versus full width at half maximum (FWHM) of XRD peak was examined, as shown in Fig. 12. The green color presents nanohardness evolution, and the blue and red colors present FWHM in axial and hoop directions, respectively. Nanohardness measurements showed a hard region in the first 12 µm, then a soft region over a 30 µm depth and then back to the base material hardness. FWHM values decreased significantly in the first 15 µm due to the decreasing of dislocation density as confirmed by the KAM figures. Furthermore, FWHM became relatively stable at a depth of 35 µm. On the basis of these results, it can be concluded that the softening could not be related to recovery (i.e., decreasing of dislocation density) in the 15-30-µm-deep region.

The presence of a softened layer after hard turning of Inconel 718 is in agreement with the results reported by Sharman et al. (Ref 49) and by Thakur et al. (Ref 50) on turning of Inconel 718 and Incoloy 825, respectively. Frictional heat generated during machining and/or the presence of tensile residual stresses in the subsurface layers has been proposed as

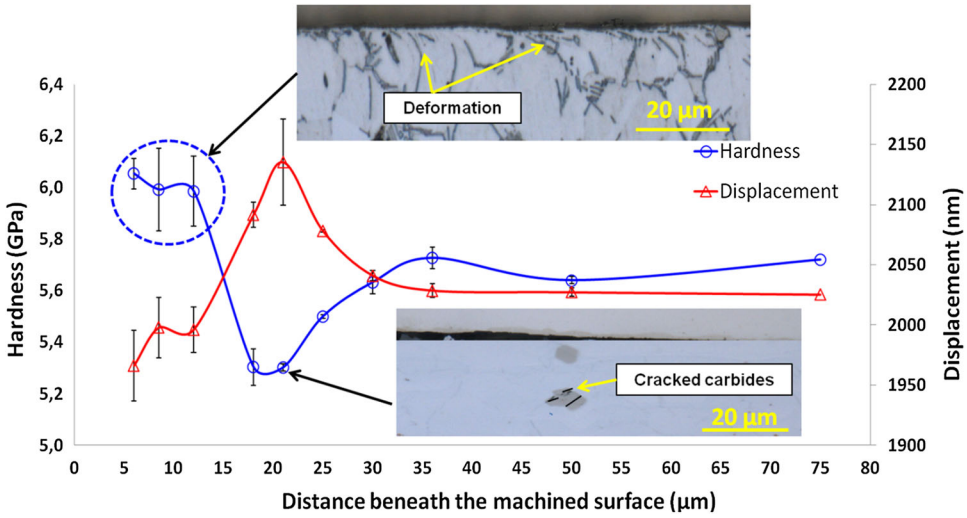

Fig. 11 Spoon-shaped curve showing the evolution of nanohardness beneath the machined surface of hard turned Inconel 718

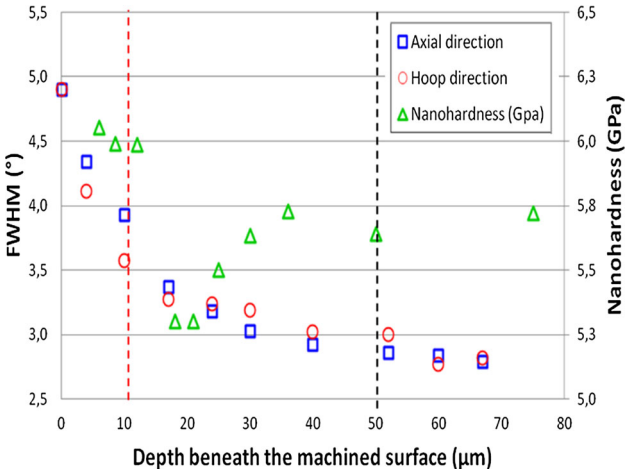

Fig. 12 Nanohardness evolution in the subsurface vs. FWHM values

possible mechanisms for the formation of the softened layer. In addition to the above factors, the low thermal conductivity of the Inconel 718 (11 Wm K^{-1}) contributes also to the thermal softening process by conserving the heat in the subsurface layers during machining. However, quantifying the contribution of each of the above mechanisms appears to be very complex as they all occur at the same time.

The enhancement of hardness in heat-treated nickel superalloys is related to the presence of secondary phases and (Ti, Nb) C carbide particles (Ref 51-53). The results obtained in the present investigation showed that cracked carbides were concentrated in the subsurface layer at a depth corresponding to the softened region, as shown in Fig. 6(a), (b) and (c), and 7(a) and (b), and the average of cracked carbide of the affected area was determined to be 20.5%. EBSD results showed that the region comprised between 12 and 25 µm depth presented a high gradient of Schmid factor and KAM misorientations. The presence of this gradient at this specific depth is probably the main factor leading to the shearing of the hard carbides located between 12 and 25 µm depth, as shown in Fig. 11. These levels of deformation could also lead to the shearing of secondary phases resulting to the observed local softening.

Finally, it must be that the depth of the softened layer is expected to change with the cutting conditions, and therefore, the amount of the cracked carbides will be changed too. However, an in-depth study of this aspect was not in the scope of the present work, and therefore, we limited ourselves to highlight its importance for future work.

3. Conclusions

In this study, a combination of laser confocal, EBSD and in situ SEM nanoindentation was used to characterize the subsurface layer of hard turned Inconel 718 and propose possible governing mechanisms for the observations. Experimental analysis of Inconel 718 machined samples has documented the mechanisms responsible for the appearance of cracked carbides in the surface and especially in the subsurface layer. In addition, the following conclusions can be drawn from the study:

- Softening layer was identified using nanoindentation measurements. Microstructure characterization confirms that the position of the cracked carbides corresponds also to a local softening on the subsurface microstructure
- Carbides above a threshold size of 3 µm are easier to be cracked than the smaller ones.
- Cracks become denser when the carbide size increases and the cracking appears to occur during rotation of the large carbides under the effect of material shearing.
- A combination of high gradient of Schmid factor and high local kernel average misorientation in the adjacent grains indicates to be the leading cause of cracking of (Ti, Nb) C carbides located at the grain boundaries of the affected layer.

Further work is underway to correlate machining process parameters with the characteristics of the cracked carbides in the subsurface layer and relate these characteristics to service life properties.

Acknowledgments

The above work was carried out under the CRIAQ project MANU 510. The authors would like to acknowledge the National Science and Engineering Research Council NSERC, Mitacs, Pratt & Whitney Canada and Heroux-Devtek for their support. The first author also appreciates the efforts of Dr. Morteza Sadeghifar for performing XRD measurements.

References

1. E.O. Ezugwu, J. Bonney, and Y. Yamane, An Overview of the Machinability of Aeroengine Alloys, *J. Mater. Process. Technol.*, 2003, **134**(2), p 233–253
2. C.M. Kuo et al., Aging Effects on the Microstructure and Creep Behavior of Inconel 718 Superalloy, *Mater. Sci. Eng. A*, 2009, **510–511**, p 289–294
3. A. Thomas et al., High Temperature Deformation of Inconel 718, *J. Mater. Process. Technol.*, 2006, **177**(1–3), p 469–472
4. S. Ghosh, S. Yadav, and G. Das, Study of Standard Heat Treatment on Mechanical Properties of Inconel 718 Using Ball Indentation Technique, *Mater. Lett.*, 2008, **62**(17–18), p 2619–2622
5. A. Chamanfar et al., Microstructural Characteristics of Forged and Heat Treated Inconel-718 Disks, *Mater. Des.*, 2013, **52**, p 791–800
6. G.A. Rao et al., Effect of Standard Heat Treatment on the Microstructure and Mechanical Properties of Hot Isostatically Pressed Superalloy Inconel 718, *Mater. Sci. Eng. A*, 2003, **355**(1–2), p 114–125
7. R.M. Arunachalam, M.A. Mannan, and A.C. Spowage, Surface Integrity When Machining Age Hardened Inconel 718 with Coated Carbide Cutting Tools, *Int. J. Mach. Tools Manuf*, 2004, **44**(14), p 1481–1491
8. M. Rahman, W.K.H. Seah, and T.T. Teo, The Machinability of Inconel 718, *J. Mater. Process. Technol.*, 1997, **63**(1), p 199–204
9. J.M. Zhou, V. Bushlya, and J.E. Stahl, An Investigation of Surface Damage in the High Speed Turning of Inconel 718 with Use of Whisker Reinforced Ceramic Tools, *J. Mater. Process. Technol.*, 2012, **212**(2), p 372–384
10. D. Dudzinski et al., A Review of Developments Towards Dry and High Speed Machining of Inconel 718 Alloy, *Int. J. Mach. Tools Manuf*, 2004, **44**(4), p 439–456
11. G. Brandt, A. Gerendas, and M. Mikus, Wear Mechanisms of Ceramic Cutting Tools When Machining Ferrous and Non-ferrous Alloys, *J. Eur. Ceram. Soc.*, 1990, **6**(5), p 273–290
12. E.O. Ezugwu, Z.M. Wang, and A.R. Machado, The Machinability of Nickel-Based Alloys: A Review, *J. Mater. Process. Technol.*, 1999, **86**(1), p 1–16

13. Q. Huang and J.X. Ren, Surface Integrity and Its Effects on the Fatigue Life of the Nickel-Based Superalloy GH33A, *Int. J. Fatigue*, 1991, **13**(4), p 322–326
14. M. Krook, V. Recina, and B. Karlsson. Material Properties Affecting the Machinability of Inconel 718, in *Proceedings of the 6th International Special Emphasis Symposium "Superalloys"* (2005)
15. L. Chen, T.I. El-Wardany, and W.C. Harris, Modelling the Effects of Flank Wear Land and Chip Formation on Residual Stresses, *CIRP Ann.*, 2004, **53**(1), p 95–98
16. T. Kitagawa, A. Kubo, and K. Maekawa, Temperature and Wear of Cutting Tools in High-Speed Machining of Inconel 718 and Ti·6Al·6 V·2Sn, *Wear*, 1997, **202**(2), p 142–148
17. W. Li et al., Effect Tool Wear During End Milling on the Surface Integrity and Fatigue Life of Inconel 718, *Procedia CIRP*, 2014, **14**(Supplement C), p 546–551
18. J.M. Zhou et al., Effects of Tool Wear on Subsurface Deformation of Nickel-Based Superalloy, *Procedia Eng.*, 2011, **19**, p 407–413
19. B. Ozcelik, H. Oktem, and H. Kurtaran, Optimum Surface Roughness in End Milling Inconel 718 by Coupling Neural Network Model and Genetic Algorithm, *Int. J. Adv. Manuf. Technol.*, 2005, **27**(3), p 234–241
20. R.S. Pawade and S.S. Joshi, Multi-objective Optimization of Surface Roughness and Cutting Forces in High-Speed Turning of Inconel 718 Using Taguchi Grey Relational Analysis (TGRA), *Int. J. Adv. Manuf. Technol.*, 2011, **56**(1), p 47–62
21. S.K. Tamang and M. Chandrasekaran, Integrated Optimization Methodology for Intelligent Machining of Inconel 825 and Its Shop-Floor Application, *J. Braz. Soc. Mech. Sci. Eng.*, 2017, **39**(3), p 865–877
22. P.R. Provencher and M. Balaziski, Automatic Identification of Feed Marks in Machined Surface Roughness Profiles by Correlating Random Variations, *Int. J. Adv. Manuf. Technol.*, 2015, **82**(5–8), p 1305–1315
23. P.R. Provencher and M. Balazinski, Principal Component Idealizations of the Dominant Modes of Variability in the Mechanics of the Cutting Process in Metal Turning, *Int. J. Adv. Manuf. Technol.*, 2018, **95**(5), p 1665–1676
24. D. Ulutan et al., Empirical Modeling of Residual Stress Profile in Machining Nickel-Based Superalloys Using the Sinusoidal Decay Function, *Procedia CIRP*, 2014, **13**, p 365–370
25. D. Ulutan, B. Erdem Alaca, and I. Lazoglu, Analytical Modelling of Residual Stresses in Machining, *J. Mater. Process. Technol.*, 2007, **183**(1), p 77–87
26. J. Zhou et al., Analysis of Subsurface Microstructure and Residual Stresses in Machined Inconel 718 with PCBN and Al_2O_3-SiC_w Tools, *Procedia CIRP*, 2014, **13**, p 150–155
27. E. Capello, Residual Stresses in Turning: Part I: Influence of Process Parameters, *J. Mater. Process. Technol.*, 2005, **160**(2), p 221–228
28. A.R.C. Sharman, J.I. Hughes, and K. Ridgway, An Analysis of the Residual Stresses Generated in Inconel 718™ When Turning, *J. Mater. Process. Technol.*, 2006, **173**(3), p 359–367
29. S. Ranganath, C. Guo, and S. Holt, Experimental Investigations into the Carbide Cracking Phenomenon on Inconel 718 Superalloy Material, in *ASME 2009 International Manufacturing Science and Engineering Conference*, vol 2, **2**(MSEC2009-84085) (2009), pp. 33–39
30. Y. Long et al., *Multi-phase FE Model for Machining Inconel 718.* **49460**, pp. 263–269 (2010)
31. H. Touazine et al., Modeling of the Microstructure Alteration Induced by Hard Turning of Inconel 718, *Int. J. Adv. Manuf. Technol.*, 2017, **93**(9), p 3705–3712
32. H. Touazine, M. Jahazi, and P. Bocher, Accurate Determination of Damaged Subsurface Layers in Machined Inconel 718, *Int. J. Adv. Manuf. Technol.*, 2017, **88**(9), p 3419–3427
33. D. Texier et al., Crack Initiation Sensitivity of Wrought Direct Aged Alloy 718 in the Very High Cycle Fatigue Regime: The Role of Non-metallic Inclusions, *Mater. Sci. Eng. A*, 2016, **678**, p 122–136
34. S. Ranganath, C. Guo, and P. Hegde, A Finite Element Modeling Approach to Predicting White Layer Formation in Nickel Superalloys, *CIRP Ann.*, 2009, **58**(1), p 77–80
35. Y. Guo and S. Anurag, *Particle Rotations During Plastic Deformation in Hard Turning and Grinding*. (Society of Manufacturing Engineers, 2000)
36. J. Laigo et al., SEM, EDS, EPMA-WDS and EBSD Characterization of Carbides in HP Type Heat Resistant Alloys, *Mater. Charact.*, 2008, **59**(11), p 1580–1586
37. S. Birosca, The Deformation Behaviour of Hard and Soft Grains in RR1000 Nickel-Based Superalloy, in *IOP Conference Series: Materials Science and Engineering* (IOP Publishing, 2015)
38. W.Z. Abuzaid et al., Slip Transfer and Plastic Strain Accumulation Across Grain Boundaries in Hastelloy X, *J. Mech. Phys. Solids*, 2012, **60**(6), p 1201–1220
39. Z.J. Zhang et al., Fatigue Cracking at Twin Boundaries: Effects of Crystallographic Orientation and Stacking Fault Energy, *Acta Mater.*, 2012, **60**(6), p 3113–3127
40. R. Jiang, N. Gao, and P.A.S. Reed, Influence of Orientation-Dependent Grain Boundary Oxidation on Fatigue Cracking Behaviour in an Advanced Ni-Based Superalloy, *J. Mater. Sci.*, 2015, **50**(12), p 4379–4386
41. H. Agrawal et al., Rotations of Brittle Particles during Plastic Deformation of Ductile Alloys, *Mater. Sci. Eng. A*, 2002, **328**(1), p 310–316
42. S.G. Lee, Particle Cracking and Rotation during Plastic Deformation of 7075 Aluminum Alloy, *Met. Mater. Int.*, 2009, **15**(4), p 591–596
43. C. Revilla, B. López, and J.M. Rodriguez-Ibabe, Carbide Size Refinement by Controlling the Heating Rate during Induction Tempering in a Low Alloy steel, *Mater. Des. (1980–2015)*, 2014, **62**, p 296–304
44. P.P. Bhattacharjee et al., Evolution of Microstructure and Texture During Warm Rolling of a Duplex Steel, *Metall. Mater. Trans. A*, 2014, **45**(4), p 2180–2191
45. A.J. Wilkinson and T.B. Britton, Strains, Planes, and EBSD in Materials Science, *Mater. Today*, 2012, **15**(9), p 366–376
46. W. Zhang et al., Quantitative Studies of Machining-Induced Microstructure Alteration and Plastic Deformation in AISI, 316 Stainless Steel Using EBSD, *J. Mater. Eng. Perform.*, 2018, **27**(2), p 434–446
47. A. Grabulov, R. Petrov, and H.W. Zandbergen, EBSD Investigation of the Crack Initiation and TEM/FIB Analyses of the Microstructural Changes Around the Cracks Formed under Rolling Contact Fatigue (RCF), *Int. J. Fatigue*, 2010, **32**(3), p 576–583
48. S.F.D. Silva Junior et al., The Use of Magnetic Barkhausen Noise Analysis for Nondestructive Determination of Stresses in Structural Elements. in *Proceedings of the INAC 2007 International Nuclear Atlantic Conference Nuclear Energy and Energetic Challenges for 21st Century 15 Brazilian National Meeting on Reactor Physics and Thermal Hydraulics; 8 Brazilian National Meeting on Nuclear Applications* (Brazil, 2007)
49. A.R.C. Sharman, J.I. Hughes, and K. Ridgway, Workpiece Surface Integrity and Tool Life Issues When Turning Inconel 718™ Nickel Based Superalloy, *Mach. Sci. Technol.*, 2004, **8**(3), p 399–414
50. A. Thakur, A. Mohanty, and S. Gangopadhyay, Comparative Study of Surface Integrity Aspects of Incoloy 825 during Machining with Uncoated and CVD Multilayer Coated Inserts, *Appl. Surf. Sci.*, 2014, **320**(Supplement C), p 829–837
51. A. Narayan Singh et al., Effect of Thermal Aging on Microstructure, Hardness, Tensile and Impact Properties of Alloy 617, *Mater. Sci. Eng. A*, 2018, **710**(Supplement C), p 47–56
52. P. Maj et al., The Precipitation Processes and Mechanical Properties of Aged Inconel 718 Alloy After Annealing, *Arch. Metall. Mater.*, 2017, **62**, p 1695–1702
53. A. Thomas et al., High Temperature Deformation of Inconel 718, *J. Mater. Process. Technol.*, 2006, **177**(1), p 469–472